Orientation and grain-boundary dependence of shock-induced plasticity and transformation in nanocrystalline Ti

L. Wang,[1] B. Li,[2] X. L. Deng,[2] W. R. Jian,[3] M. Shang,[1] L. Deng,[1] X. M. Zhang,[1,*] J. F. Tang,[1,†] and W. Y. Hu[4]

[1]*College of Science, Hunan Agriculture University, Changsha 410128, People's Republic of China*

[2]*National Key Laboratory for Shock Wave and Detonation Physics Research, Institute of Fluid Physics, China Academy of Engineering Physics, Mianyan 621900, People's Republic of China*

[3]*Department of Mechanical Engineering, University of California at Santa Barbara, Santa Barbara, California 93106, USA*

[4]*College of Material Science and Engineering, Hunan Unviersity, Changsha, Hunan 410082, People's Republic of China*

(Received 13 March 2019; revised manuscript received 24 April 2019; published 10 May 2019)

The plasticity and $\alpha \rightarrow \omega$ transformation are important for the toughness and ductility of hcp titanium under shock loading. However, three questions remain outstanding: (i) what mechanisms govern the plasticity and transformation, (ii) how does the microstructure, i.e., grain boundaries (GBs) and crystallographic orientations, affect them, and (iii) does the transformation take place dependent on the plasticity, such as dislocation slips? We conduct large-scale nonequilibrium molecular dynamics simulations to study shock-induced plasticity and phase transformation in hexagonal columnar nanocrystalline Ti. Significant anisotropy and strong dependence on crystallographic orientation are presented during shock-induced plasticity and phase transformation. The shock first prompts "heterogeneous" dislocation slips and 90° lattice reorientation, via coupling deformation twinning and slips. Then, the on-going plastic deformation induces a "heterogeneous" $\alpha \rightarrow \omega$ phase transformation at lower impact velocities or a "homogeneous" solid-state disordering at higher impact velocities. The phase transformation mostly obeys the TAO-1 pathways originated from GBs, while a few of them are governed by Silcock mechanisms within the grains. The TAO-1 and Silcock-governed transformations stem from the emission and propagation of basal-prismatic and prismatic stacking faults, respectively. At the release/tension stage, a $\omega \rightarrow \alpha$ transformation occurs, acting as the reversed process of the $\alpha \rightarrow \omega$ transformation at the compression stage. Meanwhile, structural recovery and spallation initiate in the extending tension area induced by the release fans. Serving as the nucleation of the plasticity, phase transformation, and spallation, GBs play the key role during the loading.

DOI: 10.1103/PhysRevB.99.174103

I. INTRODUCTION

To understand the plastic deformation of metals under shock loading, with the high-stress and high-strain rate ($\dot{\epsilon} \sim 10^5$–$10^7\ s^{-1}$), is of great interest and critical to materials. Titanium (Ti), a representative hexagonal close-packed (hcp) metal, and its alloys have attractive properties, such as low density, high strength-to-weight ratio, high melting point, excellent biocompatibility, and high corrosion resistance [1–3]. Thus, they are widely applied in the aerospace, nuclear, and automotive technologies [4]. The gas-gun plate impact [5], rather than split Hopkinson pressure bar (SHPB) with $\dot{\epsilon} \sim 10^2$–$10^4\ s^{-1}$ [6], is commonly used to study the shock response of materials in experiments. Recently, the shock response of polycrystal or single-crystal Ti [7,8] in plate impact experiments has been investigated. However, a series of complex physical processes, such as plastic slips [9] and their interactions, twinning [10] nucleation and growth, and phase transformation [11], involved in the shock response of materials is difficult to detect in such experiments. Consequently, the modeling in mesoscale [12,13] or atomic scale [14] is implemented to simulate the details of deformation, e.g., dislocation propagations and movements, of polycrystal or single-crystal Ti under shock loading.

The phase transformation, especially the solid-solid phase transformation, is one of the most important issues in shock science [15–18]. In hcp metals, such as zirconium (Zr) and Ti, the phase transformation can be easily activated under shock loading [11,14,19]. Upon shock compression, the hcp Zr or Ti can undergo a structural change from the α to ω phase (i.e., hcp to hexagonal crystal structure) [8,11,20,21], which is absent in hcp metals under nonshock loading, such as SHPB [9]. However, the mechanism of shock-induced transformation is still an ongoing research topic [11,22]. The experiments of Cerreta *et al.* [11] presented that the Silcock mechanism, with the orientation relations of $(0001)_\alpha//(11\bar{2}0)_\omega$ and $[11\bar{2}0]_\alpha//[0001]_\omega$, dominates the phase transformation induced by shock in Zr or Ti, which is consistent with the results of nonequilibrium molecular dynamics (NEMD) simulations [14]. But the experiments of Swinburne *et al.* [22] demonstrated that TAO-1 [23], another transformation mechanism with the lowest-energy barrier and orientation relations of $(0001)_\alpha//(0\bar{1}11)_\omega$ and $[11\bar{2}0]_\alpha//[01\bar{1}1]_\omega$, is governing the $\alpha \rightarrow \omega$ transformation in hcp metals under shock loading. Such a difference in transformation can be attributed to two factors: (i) metallic microstructures, such as crystallographic

*fengzxm_1986@163.com

†jftang@hunau.edu.cn

orientation and grain boundaries, which present strong effects on the phase transformation [14,17,24], and (ii) the experimental modes, i.e., postmortem microstructures analysis and dynamic analysis by femtosecond x-ray diffraction were carried out for the experiments of Cerreta *et al.* [11] and Swinburne *et al.* [22], respectively. In the shock experiment, a reversed $\omega \rightarrow \alpha$ transformation [8] is commonly prompted during unloading, but the mechanism for such transformation is unknown. Consequently, the first goal of this work is to reveal the phase transformation, including forward and reversed transformation, in Ti under shock loading, including their dynamic processes, the corresponding mechanisms, and their dependence on the orientation and grain boundaries (GBs).

Actually, the study of plastic deformation [9], in the hcp metals such as Ti or Zr, is another challenge. Fortunately, the crystallography and quantitative analysis in experiments, i.e., the measurement of transmission electron microscopy (TEM) [11], electron backscattered diffraction (EBSD) [8,25,26], and neutron diffraction [27], on the plasticity in hcp metals have been employed extensively. The plastic deformation in hcp metals consists of two key modes, i.e., dislocation slip and deformation twinning. Under nonshock loading, the plasticity, especially deformation twinning, in hcp metals presented significant dependences on the loading conditions, such as the straining condition [25]. For instance, $\{10\bar{1}2\}$ and $\{11\bar{2}1\}$ twins are predominant at small strains, while another twinning mode, the $\{11\bar{2}2\}$ twin, can also be activated at higher strains [25] for a compressed Zr. Still, what is the plastic deformation in hcp metals under shock loading and what is the underlying mechanism? This remains largely unexplored and a description of dynamic behaviors in the atomic scale is needed. In addition, the plastic deformation is also dependent on the microstructures (i.e., crystallographic orientation and GB characteristics) during dynamic loading [28,29]. However, the investigation of the microstructure dependence of plastic deformation, i.e., its nucleation, dynamic evolution, and the corresponding mechanisms, in hcp metals such as Ti, under shock loading, is rare. This is due to the difficulties in carrying out *in situ* measurement of shock-induced plastic deformation, with the transient loading time of the order of tens to hundreds of nanoseconds, and complicated microstructures. Consequently, the other goal of this work is to explore the plasticity in α-Ti consisting of a series of GBs and crystallographic orientations under shock loading, and reveal the theoretical relationship between plasticity and microstructures.

Recently, time-resolved x-ray diffraction analysis, applied in both MD simulations and shock experiments [5,30], highlighted the effects of microstructure on plastic deformation. To gain more insights into the shock-induced deformation mechanism, it is necessary to resolve the microstructure via *in situ* and real-time electron/x-ray imaging and diffraction. Comparing with the data from experiments and MD simulations, one can relate the atomic evolutions to the specific diagnostic results and interpret the experimental information better. In this work, we conduct large-scale NEMD simulations to investigate the dynamic deformation of columnar nanocrystalline Ti with different GB characteristics. Orientation mapping (OM), slip vectors, and simulated electron diffraction are utilized to analyze the atomic evolution, which reveals significant anisotropy and strong crystallographic orientation dependence under extreme shock loading. Plastic deformation originates from GBs and GB junctions during shock compression, while structural recovery and spallation are also induced at GBs during the release and tension stage. The simulation model and methodology are described in Sec. II, and results and discussion in Sec. III, followed by the summary and conclusions in Sec. IV.

II. MODEL AND METHODOLOGY

A. The details of models and simulations

For our NEMD simulations, the large-scale atomic/molecular massively parallel simulator (LAMMPS) [31] and modified embedded atom method (MEAM) potential of Ti [32] are utilized. This potential can accurately describe the plastic properties [33] and the $\alpha \rightarrow \omega$ transformation of Ti [14], verified by density functional theory, tight-binding, and experimental results [34]. This potential also presents a reasonable accuracy for shock simulations. To check the performance of such MEAM potential during shock loading, we carry out simulations under different shock strengths along different crystallographic orientations in single-crystal Ti. Here we choose the x axis, parallel to the $[1\bar{2}10]$, $[10\bar{1}0]$, or [0001] crystallographic directions of the Ti crystal, as the impact direction. The dimensions of the single-crystal Ti are about $12 \times 12 \times 140\,\mathrm{nm}^3$ ($\sim$1.1 million atoms), and the impact velocities u_p range from 0.75 to 3.0 km s^{-1}, corresponding to the pressure of $P = 22.6$–106.9 GPa. Based on the propagation profiles of u_p [Fig. 1(a)], the relation between shock velocity u_s and shock-state particle velocity u_p is obtained. The u_s–u_p relations of the plastic shocks (P1) for single-crystal Ti, shocked along $[1\bar{2}10]$, $[10\bar{1}0]$, and [0001], respectively, are shown in Fig. 1(b), which are in agreement with the theoretical [14] and experimental results [35]. The functions of pressure vs normalized specific volume (V/V_0) are shown in Fig. 1(c). Despite the scatter in the experimental data, our simulations results are consistent with the experiments for the compression ($1 - V/V_0$) ranging from 10% to 40%. It presents a reasonable accuracy of this potential for shock simulations from the results above, although its accuracy for deformation at high pressure ($u_\mathrm{p} > 3.0$ km s^{-1}) remains to be established.

During shock loading in single-crystal Ti, a two-wave profile is observed as shock along the $[1\bar{2}10]$, consisting of a plastic wave, which overtakes the elastic wave, and a transformation wave, different from the common elastic-plastic wave structure; while an interesting three-wave structure is observed, as shock along $[10\bar{1}0]$ and [0001] at the intermediate strengths [Fig. 1(a)], from the shock propagation profiles of $u_\mathrm{p}(x)$, similar to that from experimental measurement using the velocity interferometer system for any reflector (VISAR) [36]. The shock front consists of an elastic precursor (E), a plastic wave (P1), and a phase transformation wave (P2). At the stage of P1, deformation twinning is predominant and facilitates the rotation of parent α to the product α' phase (e.g., $[10\bar{1}0]$-α rotates to the [0001]-α' variant); while the $\alpha \rightarrow \omega$ phase transformation, obeying

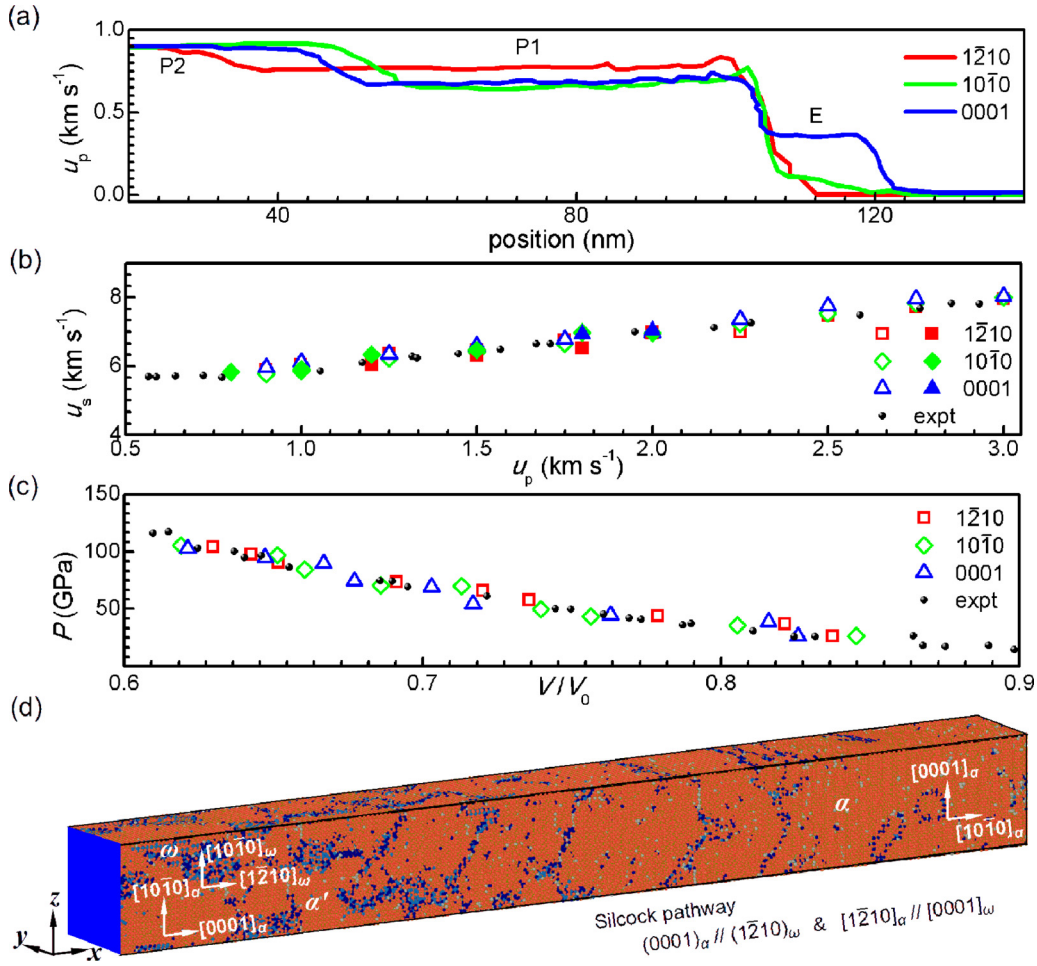

FIG. 1. (a) Particle velocity profile $u_p(x)$ for shock loading along $[10\bar{1}0]$, at $t = 14$ ps. E: elastic wave; P1: plastic wave; P2: phase transformation wave. (b) The u_s–u_p plots obtained from our MD simulations (open symbols), and previous simulations [14] (filled symbols), and experiments (black dots) [35], and (c) the corresponding plots of pressure (P) vs normalized specific volume (V/V_0). (d) Shock-induced plasticity and transformation in single-crystal Ti. It exhibits stronger similarities to the experiments [11] and previous MD simulations [14], i.e., the phase transformation is governed by the Silcock mechanism, with orientation relationships (ORs) of $(0001)_\alpha$ // $(1\bar{2}10)_\omega$ and $[1\bar{2}10]_\alpha$// $[0001]_\omega$, rather than TAO-1, i.e., ORs of $(0001)_\alpha$ // $(10\bar{1}1)_\omega$ and $[1\bar{2}10]_\alpha$ // $[10\bar{1}1]_\omega$. Here, the single-crystal Ti shocked along the $[10\bar{1}0]$ directions ($t = 22$ ps) at $u_p = 0.75$ km s^{-1} is taken as the example. Comparing with the results of nanocrystalline Ti (Figs. 9 and 15), it reveals a strong dependence of grain boundaries for shock-induced transformation.

the Silcock pathway [37] with orientation relationships (ORs) $(0001)_\alpha$ // $(1\bar{2}10)_\omega$ and $[1\bar{2}10]_\alpha$ // $[0001]_\omega$, occurs at the stage of P2 [Fig. 1(d)]. However, the TAO-1 mechanism for the phase transformation (ORs: $(0001)_\alpha$ // $(10\bar{1}1)_\omega$ and $[1\bar{2}10]_\alpha$ // $[10\bar{1}1]_\omega$) with the lowest barrier energy [23] cannot arise. Similar phenomena have also been obtained in previous MD simulations [14]. The above results demonstrate that the MEAM potential is appropriate to be applied in shock simulations.

A Voronoi tessellation method [38] is then used to construct an idealized hexagonal columnar nanocrystalline microstructure unit, containing six grains of identical hexagonal shape and diameter within the three-dimensional (3D) periodic cell. The grain diameter is about 20 nm. The columnar axis is along the [0001] crystallographic direction (z axis) and the thickness along this axis is about 36 nm. Three types of grains are included, which are denoted as A, B, and C [Fig. 2(a)], respectively. They are oriented relative to the x axis ($[10\bar{1}0]$ in B) by an angle of $\phi = -30°$, $0°$, and $30°$, respectively. Then this unit configuration is replicated two times along the x axis, adding six grains. The dimensions of the resulting configuration are about $102 \times 30 \times 36$ nm, containing approximately 6 million atoms. The configurations are first relaxed at 0 K with the conjugate gradient method, and then thermalized at the ambient conditions with a constant-pressure-temperature ensemble and 3D periodic boundary conditions, prior to shock loading. Thermal-induced GB migrations are observed owing to their instabilities, leading to the change of grain shape (Fig. 2). Shock simulations are then performed with the microcanonical ensemble. Periodic boundary conditions are applied along the y and z axes, while a free boundary is applied along the x axis. The time step for integration of the equation of motion is 1 fs, and the run duration is 58 ps. The small region on the left is set as the piston [39] in our shock simulations. The interactions between the piston and the rest of the atoms in the configuration are described with the same interatomic potential, while the atoms in the piston do not participate in molecular dynamics. An

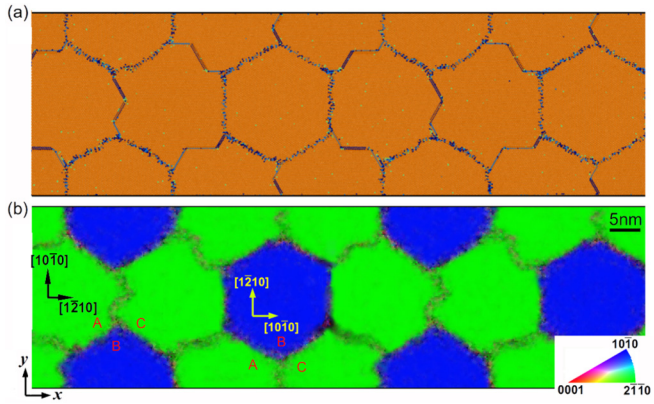

FIG. 2. Configurations of hexagonal columnar nanocrystalline Ti projected onto (0001), color-coded with (a) CNA and (b) orientation map along the x axis. The dimensions of the configuration are about 102 × 30 × 36 nm, consisting of about 6 million atoms. Shock direction: left → right, along the x axis. A-, B-, and C-type grains represent those oriented relative to the [10$\bar{1}$0] direction by an angle $\phi = -30^\circ$, 0°, and 30° around the z axis ([0001] direction), respectively.

atomic piston delivers the shock with the piston velocity of u_p, ranging from 0.5 to 2.0 km s^{-1}, starting at time $t = 0$ from $x = 0$ along the x axis towards the free surface. At $t =$ 30 ps, the piston is stopped, creating a release fan propagating toward the free surface. This release fan interacts with that due to the shock reflection from the surface, and induces release and subsequent tension within the target interior [40].

B. Analysis methodology

To describe the response during shock loading, we perform the 1D and 2D binning analyses [40], resolving spatially physical properties such as stresses σ_{ij} ($i = x, y, z$). The bin width is 0.5 nm. The center-of-mass velocity $\bar{v}_i$ of a bin is removed when calculating σ_{ij} within each bin: $\Delta\sigma_{ij} = -(m/V_a)\bar{v}_i\bar{v}_j$, where m is the atomic mass and V_a is the atomic volume averaged over the bin. The pressure is obtained as

$$P = \frac{\sigma_{xx} + \sigma_{yy} + \sigma_{zz}}{3}, \tag{1}$$

while the shear stress τ is defined as

$$\tau = \frac{1}{2}\left[\sigma_{xx} - \frac{1}{2}(\sigma_{yy} + \sigma_{zz})\right]. \tag{2}$$

To characterize the microstructure deformation, the common neighbor analysis (CNA) [41], slip vectors methods [28,42], and electron diffraction in a selected area [29] are also implemented. In our simulations, to better reveal orientation effects and visualize the plasticity, such as the twins within the shocked crystals, we also performed orientation mapping (OM) analysis [Fig. 2(b)] [29], following standard electron backscatter diffraction (EBSD) analysis [43]. For hcp metals, the crystal orientation with respect to a reference coordinate system is also represented by a three-dimensional orthogonal rotation matrix **R**. Thus the hexagonal coordinate crystal system should first be transformed to the orthogonal coordinate system and the three crystallographic axes in the orthogonal coordinate system, where $\boldsymbol{a}_1$: [100], $\boldsymbol{a}_2$: [010], and $\boldsymbol{a}_3$: [001] correspond to the [2$\bar{1}\bar{1}$0], [01$\bar{1}$0], and [0001] directions in the hexagonal system, respectively. Then, **R** can be defined as as the misorientation between three crystallographic axes, $\boldsymbol{a}_i$ ($i = 1$, 2, and 3), and the x, y, and z axes in the coordinate system of observation. The direction angles α_i, β_i, γ_i ($i = 1$, 2, and 3) are defined as those between $\boldsymbol{a}_i$ and the x, y, and z axes, respectively. The rotation matrix **R** is then expressed in terms of direction cosines as

$$\mathbf{R} = \begin{pmatrix} \cos\alpha_1 & \cos\beta_1 & \cos\gamma_1 \\ \cos\alpha_2 & \cos\beta_2 & \cos\gamma_2 \\ \cos\alpha_3 & \cos\beta_3 & \cos\gamma_3 \end{pmatrix}. \tag{3}$$

For a perfect hcp lattice, a set of 12 vectors, pointing from the central atom to its 12 nearest neighbors, is defined and $\hat{m}$, which is normal to the mirror plane and has a positive projection in the z axis, is chosen as a unit vector corresponding to [0001]. The vector $\hat{n}$ pointing from the central atom to one of its nearest neighbors on the mirror plane is taken as the second unit vector, corresponding to [2$\bar{1}\bar{1}$0]. Thus, the crystallographic directions $\boldsymbol{a}_i$ in the orthogonal coordinate system, corresponding to [2$\bar{1}\bar{1}$0], [01$\bar{1}$0], and [0001] in the hexagonal system, can be expressed as

$$(\boldsymbol{a}_1, \boldsymbol{a}_2, \boldsymbol{a}_3) = (\hat{n}, \hat{m} \times \hat{n}, \hat{m}). \tag{4}$$

Given $\boldsymbol{a}_i$ and the x, y, and z axes, the nine direction angles α_i, β_i, and γ_i can be obtained, and therefore rotation matrix **R** can be computed with Eq. (3). For an atom within a deformed region, there are n_{CN} direction vectors from which $\boldsymbol{a}_i$ is selected. Only the crystallites centered at an atom under consideration are deemed resolvable if $10 \leqslant n_{CN} \leqslant 14$, while other crystallites are considered as "unresolvable," similar to unresolvable areas in experimental EBSD analysis. The values of $\boldsymbol{a}_i$ for an arbitrary crystallite may deviate from those for a perfect lattice, leading to different direction angles, and **R**.

Given the **R** matrix for "each crystallite," the orientation vectors **Q**, representing the projection of the system axes, **X**, onto the crystal system, can be obtained as

$$\mathbf{Q} = \mathbf{R} \cdot \mathbf{X}, \tag{5}$$

which can also be expressed as

$$\mathbf{Q} = \begin{pmatrix} Q_1 \\ Q_2 \\ Q_3 \end{pmatrix} = \begin{pmatrix} \cos\alpha_1 & \cos\beta_1 & \cos\gamma_1 \\ \cos\alpha_2 & \cos\beta_2 & \cos\gamma_2 \\ \cos\alpha_3 & \cos\beta_3 & \cos\gamma_3 \end{pmatrix} \cdot \begin{pmatrix} X_1 \\ X_2 \\ X_3 \end{pmatrix}. \tag{6}$$

For example, the crystal system projections of the reference system axes, i.e., x, y, and z axes, can be obtained as $Q_x = (\cos\alpha_1, \cos\alpha_2, \cos\alpha_3)$, $Q_y = (\cos\beta_1, \cos\beta_2, \cos\beta_3)$, and $Q_z = (\cos\gamma_1, \cos\gamma_2, \cos\gamma_3)$, respectively.

However, the crystallographic direction for hcp systems is described with four indices in the hexagonal coordination systems, and the orientation vector of a crystallite, $\mathbf{Q}^{hex}$, can be transformed from its counterpart **Q** in the orthogonal coordinate system via

$$\mathbf{Q}^{hex} = \begin{pmatrix} Q_1^{hex} \\ Q_2^{hex} \\ Q_3^{hex} \\ Q_4^{hex} \end{pmatrix} = \begin{pmatrix} \frac{2}{3}Q_1 \\ \frac{1}{3}(\sqrt{3}Q_2 - Q_1) \\ \frac{1}{3}(Q_1 - \sqrt{3}Q_2) - \frac{2}{3}Q_1 \\ \left(\frac{c}{a}\right)^{-1}Q_3 \end{pmatrix}, \tag{7}$$

where c/a is the lattice parameter ratio for an hcp structure.

Then, a normalized vector **C**, representing the orientation in red-green-blue (RGB) color, can be obtained via

$$\mathbf{C} = (C_1, C_2, C_3) \tag{8}$$

$$= \left(Q_3, \sqrt{3}\frac{Q_2}{Q_1}\sqrt{Q_1^2 + Q_2^2}, |Q_1 - \sqrt{3}Q_2|\right), \tag{9}$$

where $0 \leqslant Q_1 \leqslant \sqrt{3}Q_2$ and $Q_3 \geqslant 0$. For digital eight-bit color, the numerical representation of the "orientation mapping" (OM) vector $\mathbf{Q}_{\mathrm{OM}}$ can be expressed as

$$\mathbf{Q}_{\mathrm{OM}} = (R, G, B) = \left(\frac{C_1}{C_{\max}}, \frac{C_2}{C_{\max}}, \frac{C_3}{C_{\max}}\right), \tag{10}$$

where $C_{\max}$ is the maximum in C_i $(i = 1, 2, 3)$. In the hcp color triangle, $\langle 0001\rangle$, $\langle 2\bar{1}\bar{1}0\rangle$, and $\langle 10\bar{1}0\rangle$ are denoted with the primary colors red, green, and blue, respectively [Fig. 2(b)].

III. RESULTS AND DISCUSSION

The NEMD simulations of shock loading in nanocrystalline Ti (nc-Ti) are performed for a range of particle velocities from 0.5 to 2.0 km s^{-1} (∼20–48 GPa). Upon shock, wave propagation and interactions undergo a series of stages in nc-Ti: the impact-induced shocks, subsequent release fans originating at free surfaces, and interaction of the opposing release fans, which yield well-defined shock compression, release, tension, and spallation.

A. Shock compression stage

1. "Heterogeneous" and "homogeneous" deformation

During compression, shocks along the x direction first induce the apparent structural deformation, i.e., the grain rotation, giving rise to the GB migration and subgrains formation, and then trigger a phase transformation at lower-impact velocities [$u_{\mathrm{p}} \leqslant 1.0$ km s^{-1}; Figs. 3(a) and 3(b)] or the disordering at higher-impact velocities [$u_{\mathrm{p}} \geqslant 1.5$ km s^{-1}; Figs. 3(c) and 3(d)]. This disordering is amorphization or solid-state disordering, rather than premelting [44]. The calculated diffusion coefficient is $D \sim 10^{-11}$–10^{-10} m^2 s^{-1}, in these amorphization regions, similar to that in solid crystal, confirming the solid state.

The compression-induced plasticity and transformation present strong dependence of the crystallographic orientation at lower-impact velocities. The plastic deformation, e.g., grain rotation [P1, Fig. 4(a)], facilitating the release of pressure and shear stress [Fig. 4(b)] prefers to arise in B-type grains, where the shock wave propagates along the x-[10$\bar{1}$0] direction [u_{p} = 0.5 and 1.0 km s^{-1}; Figs. 3(a) and 3(b)], rather than in A- or C-type grains ([1$\bar{2}$10] or [$\bar{1}\bar{1}$20] directions along the x

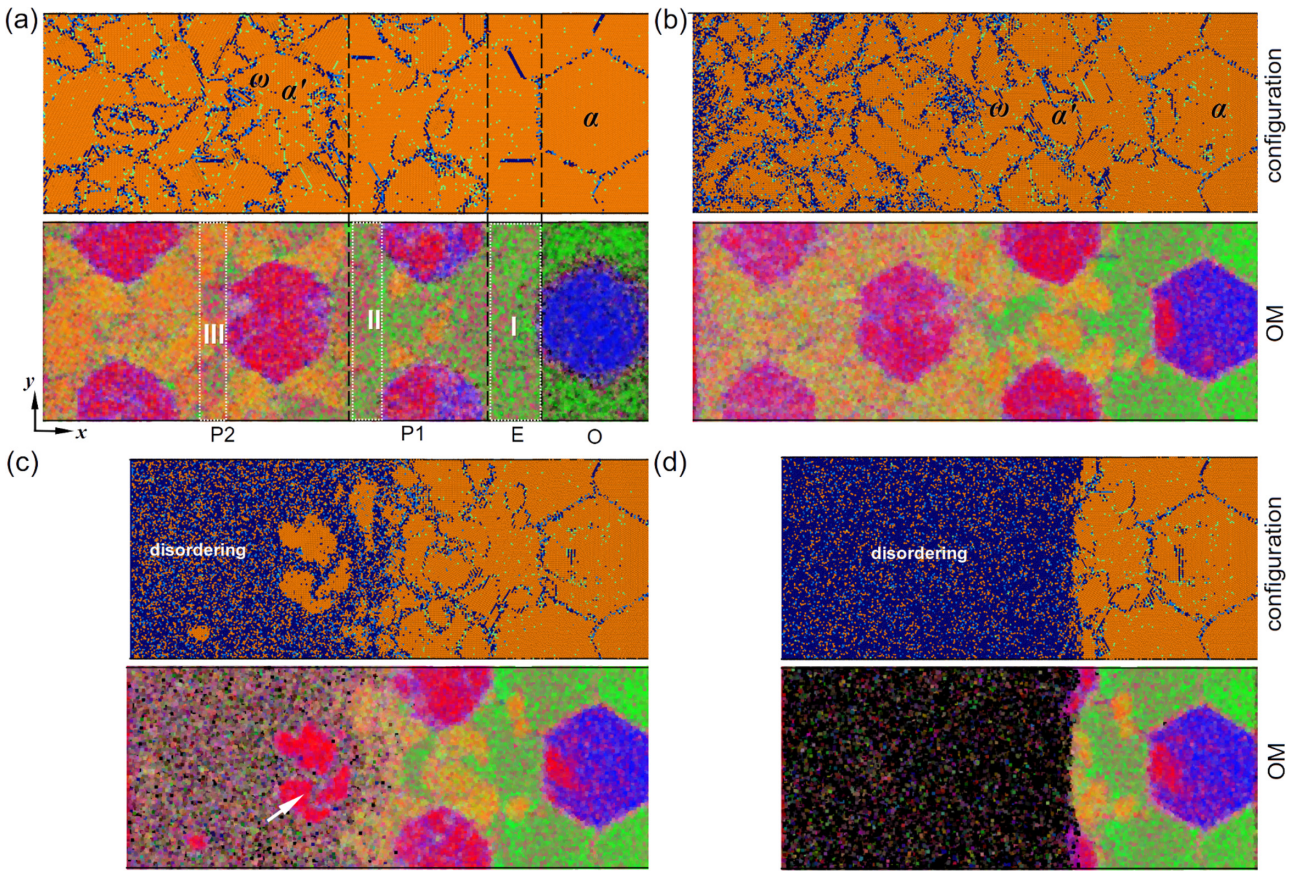

FIG. 3. Atomic configurations and the corresponding orientation maps for hexagonal columnar nc-Ti during shock compression, at u_{p} = (a) 0.5 km s^{-1} (t = 18 ps,), (b) 1.0 km s^{-1} (t = 15 ps), (c) 1.5 km s^{-1} (t = 12 ps), and (d) 2.0 km s^{-1} (t = 10 ps), respectively. O: unshocked; E: elastic wave; P1: the plastic wave after yield; P2: the stable plastic wave. Regions I, II, and III represent the domains containing A- or C-type grains only, which are also shown in Figs. 4 and 5.

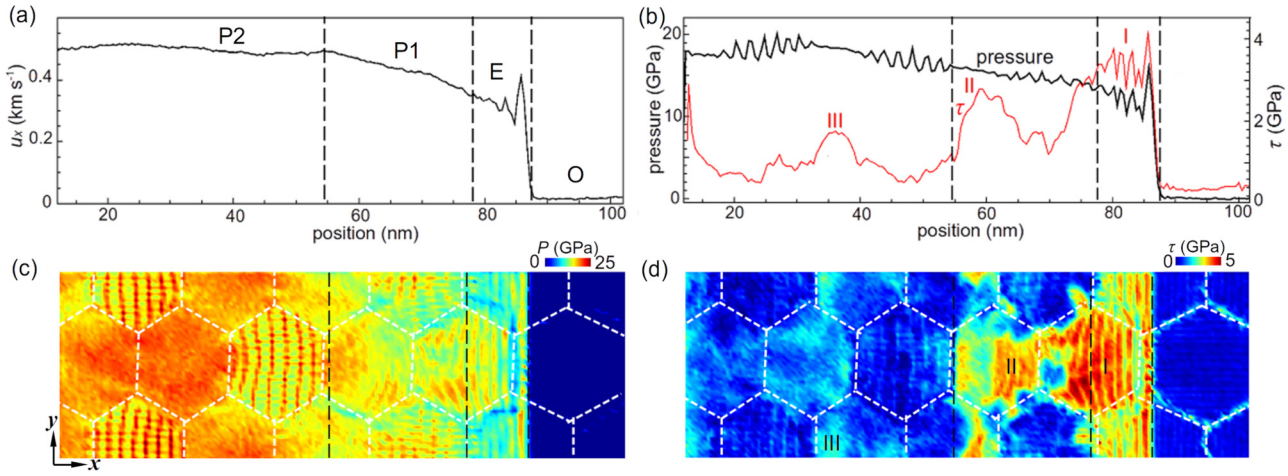

FIG. 4. The (a) particle velocity and (b) pressure P (and shear stress τ) profiles, and the corresponding 2D distribution maps of (c) $P(x, y)$ and (d) $\tau(x, y)$ in nc-Ti under compression at $u_p = 0.5$ km s^{-1} ($t = 18$ ps).

axis, respectively). Such "heterogeneous" plasticity facilitates the stress concentration or localization [Figs. 4(c) and 4(d)] and leads to some plateaus of of the stress (e.g., τ) [II and III; Fig. 4(b)]. Upon impact, the phase transformation also exhibits strong anisotropy. Shock-induced phase transformation ($\alpha \rightarrow \omega$, P2) preferentially occurs within B-type grains after plasticity, leading to the ω structure precipitated in the α matrix [Figs. 3(a) and 3(b)].

Such an anisotropy of deformation/transformation becomes weak with increase of the impact velocities. Upon impact, the deformation mode in nc-Ti undergoes a transition, from the "heterogeneous" plasticity/transformation ($u_p \leqslant 1.0$ km s^{-1}) to "homogeneous disordering" ($u_p \geqslant 1.5$ km s^{-1}; Fig. 3). Interestingly, compression-induced "disordering" also presents a "crystallographic orientation dependence" as $u_p = 1.5$ km s^{-1}. The disordering preferentially arises within A- and C-type grains, while it presents a "resistance" within B-type grains, after the grain rotation [$\alpha \rightarrow \alpha'$; Fig. 3(c)]. By further increasing the impact velocities [$u_p = 2.0$ km s^{-1}; Fig. 3(d)], the disordering that occurs is homogeneous rather than heterogeneous. The anisotropy of plasticity and transformation would prompt an anisotropic propagation of a shock-induced plastic wave in nc-Ti, as illustrated in the position-time (x-t) diagrams (Fig. 5). During shock compression, the shock front undergoes three apparent low-pressure regions (I, II, and III), at $u_p \leqslant 1.0$ km s^{-1} [Figs. 5(a) and 5(b)]. The low-pressure regions correspond to the elastic domains I, II, and III, only consisting of A- and C-type grains [Fig. 3(a)], where higher shock strength is needed to activate the plastic deformation. Thus, higher shear stresses (τ) are presented in these regions [Fig. 4(b)]. When $u_p \geqslant 1.5$ km s^{-1}, the heterogeneous to homogeneous transition of plasticity gives rise to the homogeneous distribution of stress, such as P, accelerating the weakening and annihilation of low-pressure regions at the plastic shock front in the x-t diagrams [Figs. 5(c) and 5(d)].

Based on the simulation results above, compression-induced deformation, both the plasticity and phase transformation, such as $\alpha \rightarrow \omega$ transformation, and solid-state disordering in nc-Ti present the strong anisotropy during shock loading. However, the underlying mechanism governing such anisotropy is still unrevealed. Thus, an explicit description of deformation, i.e., the evolutionary process and interaction with the microstructure (e.g., GB and crystallographic orientation), is necessary.

2. The 90° lattice reorientation

Lattice reorientation of α (parent) $\rightarrow \alpha'$ (variant), prompting the grain rotation with a rotation angle of 90° around the $\langle 1\bar{2}10 \rangle$ axis, is a primary plastic deformation mode in nanocrystalline Ti during shock compression [Fig. 6(a)]. For such lattice reorientation, it presents the high similarities to deformation twinning, i.e., $\{10\bar{1}2\}\langle 10\bar{1}1 \rangle$ twinning [45–47], which can be manifested via analyzing diffraction patterns [Fig. 6(b)], with the development of high temporal and spatial

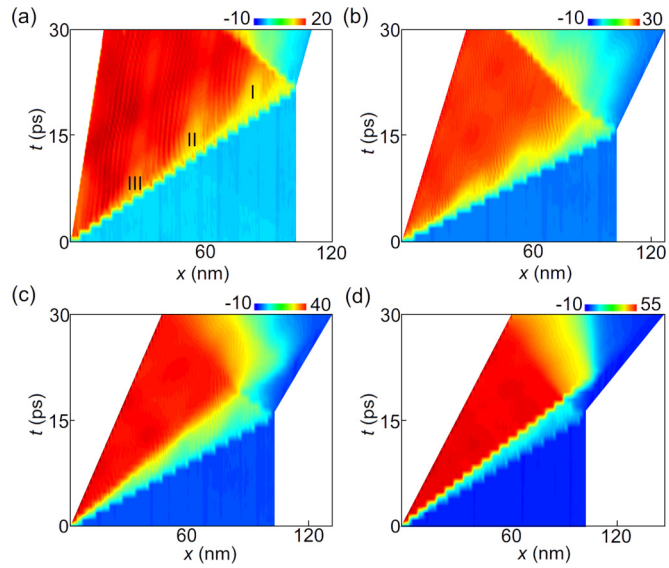

FIG. 5. Position-time (x–t) diagrams showing the wave propagation in hexagonal nc-Ti during shock compression ($t \leqslant 30$ ps) at $u_p =$ (a) 0.5 km s^{-1}, (b) 1.0 km s^{-1}, (c) 1.5 km s^{-1}, and (d) 2.0 km s^{-1}, respectively, which is color coded with pressure P (GPa).

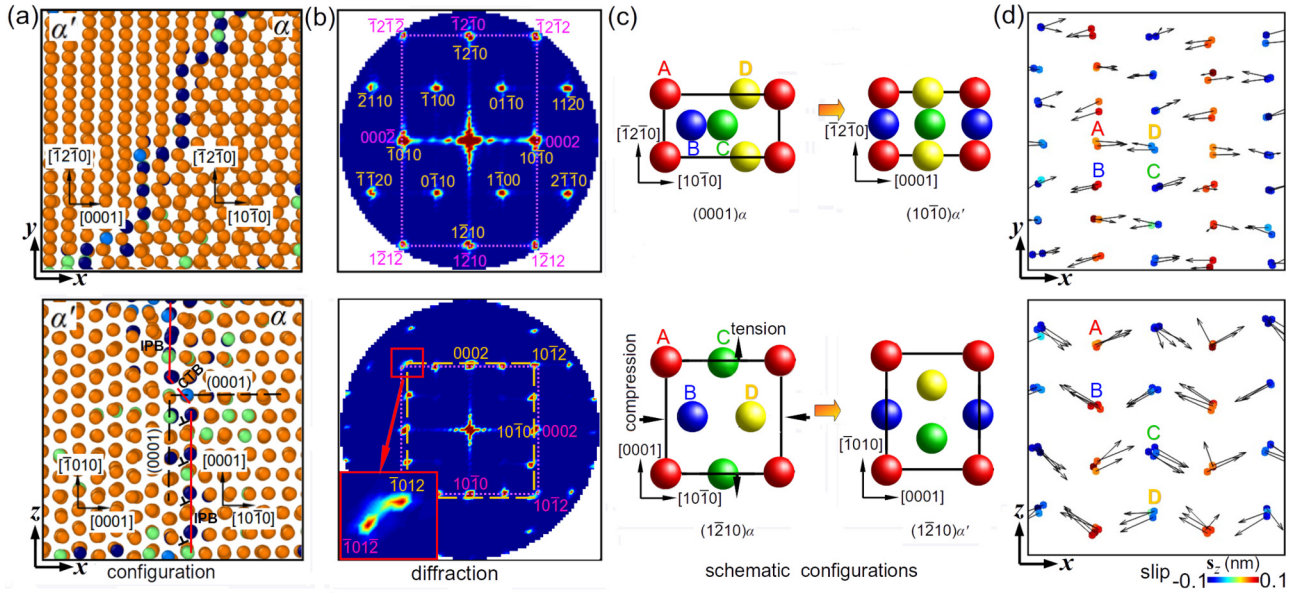

FIG. 6. (a) The lattice reorientation with a rotation angle of 90° in view of the *xy* and *xz* planes, (b) the corresponding electron diffraction patterns, where the indexes in yellow and pink represent the parent α (dashed lines) and variant α' (dotted lines), respectively and (c) its mechanism in terms of shuffle (displacement) and slip, described by the schematic illustrations, and (d) the slip vectors (colored with $\mathbf{s}_z$). Arrows show the slip directions. The symbol "⊥" denotes the partial dislocation.

resolution x-ray probes. As lattice reorientation proceeds, diffraction spots become diffused and separated in the diffraction pattern (i.e., in view of the *xz* plane), similar to that for deformation twinning [24]. However, based on the analysis of the diffraction pattern, two key differences between lattice reorientation and twinning are presented: (i) the $\bar{1}012$-α and $\bar{1}01\bar{2}$-α' spots are observed to be separated [inset, Fig. 6(b)] for lattice reorientation, while coincident for $\{10\bar{1}2\}\langle 10\bar{1}1\rangle$ twinning [24], implying lattice reorientation abandons a feature of twins, i.e., the common symmetric plane $\{10\bar{1}2\}$; and (ii) the rotation angle between the α and α' pattern (*xz* plane) is 90° for lattice reorientation, but 86.3° for twins. It implies that deformation twinning is an important mechanism for 90° lattice reorientation, but not the only mechanism. What is the mechanism governing it?

The fact is that such lattice orientation is prompted via coupling the deformation twins and slips. In hcp metals, it is observed that the lattice reorientation results from atomic shuffles [48] by atoms [A–D; Fig. 6(c)] moving along the $\langle 10\bar{1}1\rangle$ directions in the $\{10\bar{1}2\}$ planes, or the activation of $\{10\bar{1}2\}\langle 10\bar{1}1\rangle$ slip systems [Fig. 6(d)], based on the analysis of slip vectors. The shuffles facilitate the rotations of the parent hcp (α) unit cell [Fig. 7(a)] by 86.3°, leading to a $\{10\bar{1}2\}\langle 10\bar{1}1\rangle$ twinning with a misorientation angle of 86.3° [Fig. 7(b)]; while the subsequent emission of $(10\bar{1}2)[10\bar{1}1]$ slips triggers the transition from deformation twins to lattice reorientation [Fig. 7(c)] and mediates the apparent shift from the coherent twin boundary (CTB) to the incoherent prismatic-basal boundary (IPB), separating the parent α and α' [viewed along the *y* axis; Fig. 7(a)]. Such coupling effect induces a compression strain along $[10\bar{1}0]$ and a tensile strain along [0001] [Fig. 6(c)]. The compressive and tensile strains, e_{xx} and e_{zz} along the $[10\bar{1}0]$ and [0001] direction in parent α hcp, are about 5.57% and −5.79%, respectively, by evaluating the translation of diffraction spots (i.e., $10\bar{1}0$ and 0001 spots) in the patterns [Fig. 6(b)].

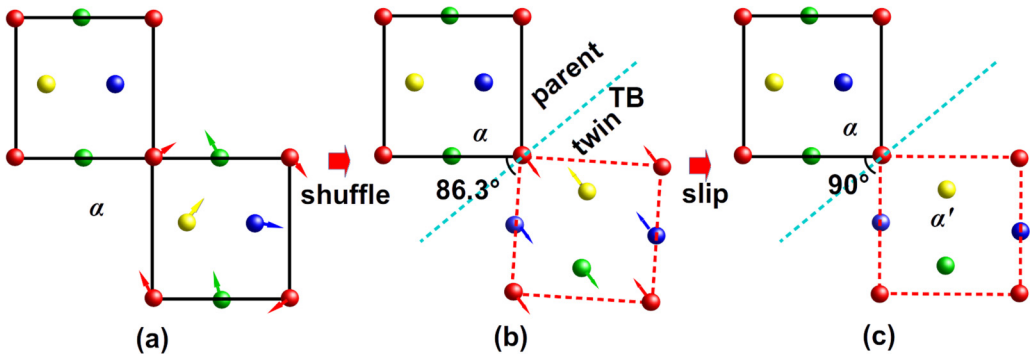

FIG. 7. Schematic illustration of the mechanism for shock-induced 90° lattice reorientation in Ti: the coupling of deformation twinning and slips. The (a) parent α-Ti, (b) deformation twin, and (c) lattice reorientation.

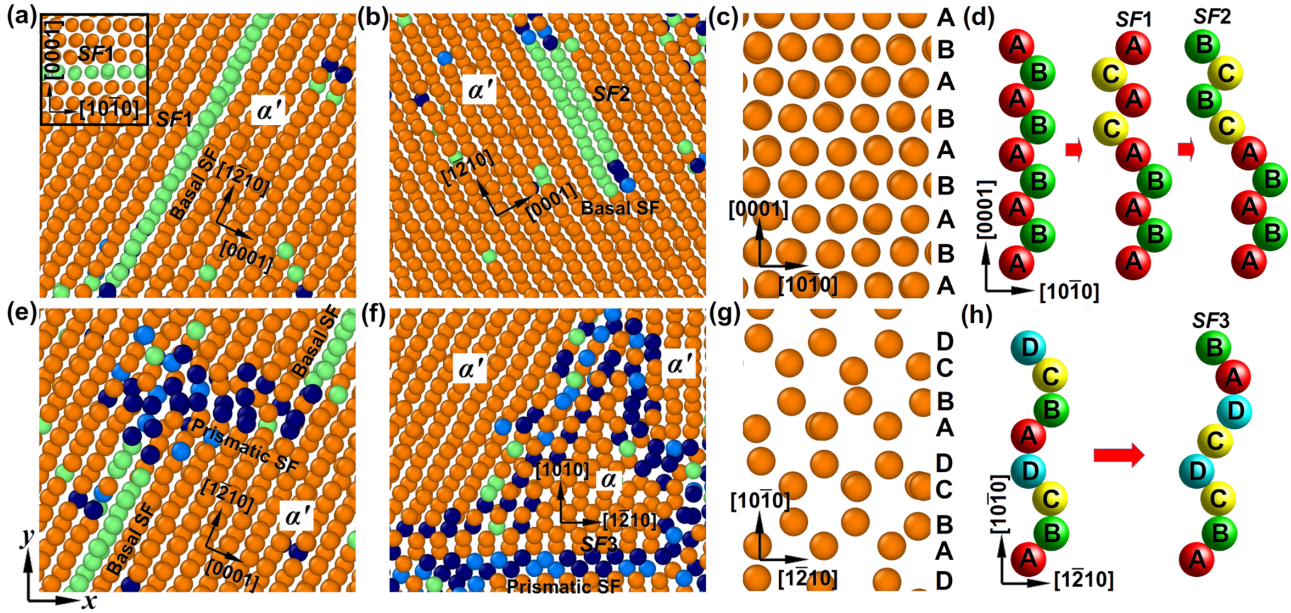

FIG. 8. Microstructural configurations showing the basal and prismatic stacking faults (SFs) within A-type grains during shock compression. (a) "Partial" basal SF ($SF1$) with a Burgers vector of $1/3[10\bar{1}0]$; (b) basal SF ($SF2$) with a Burgers vector of $1/3[1\bar{2}10]$; (c) stacking sequence of Ti in view of the $\{1\bar{2}10\}$ plane; and (d) schematic representation of the formation of $SF1$ and $SF2$. Prismatic SF with Burgers vector of $1/3[1\bar{2}10]$ ($SF3$), connected to two "partial" basal SFs, (e) in view of the $(10\bar{1}0)$ plane and (f) in view of the (0001) plane. (g) The stacking sequence of Ti in view of the (0001) plane and (h) the schematic illustration of the formation of $SF3$ in terms of the atomic layer.

3. Dislocation slips: Basal and prismatic stacking faults

The dislocation slip is another deformation mode in nc-Ti during shock compression, and two groups of dislocations, i.e., the basal (green) and prismatic (dark blue) stacking faults (SFs; Fig. 8), are emitted. The basal SFs on the (0001) plane, the most common defects in hcp metals reported by TEM studies [49], are prompted via relative slips of atoms in the variant region (α'), following the lattice reorientation. Two different basal SFs are included: the "partial" basal SF ($SF1$), with a faulted plane of stacking, i.e., the (0001) plane [green; Fig. 8(a)], and the basal SF ($SF2$), involved by two faulted planes [Fig. 8(b)]. When the unfaulted stacking sequence $\cdots$ABABABAB$\cdots$ on the $(1\bar{2}10)$ plane in hcp Ti [Fig. 8(c)] has changed into $\cdots$ABABACAC$\cdots$, $SF1$, with the Burgers vector of $1/3[10\bar{1}0]$, is formed; while the stacking sequence changes into $\cdots$ABABACBC$\cdots$, $SF2$, with the Burgers vector of $1/3[1\bar{2}10]$, are created [Fig. 8(d)]. Actually, $SF2$ can be dissociated into two $SF1$ [50], and

$$1/3[1\bar{2}10]_{SF2} \rightarrow 1/3[0\bar{1}10]_{SF1} + 1/3[1\bar{1}00]_{SF1}. \quad (11)$$

Upon impact, it also triggers another type of SF on the prismatic plane, i.e., the $(10\bar{1}0)$ plane, named the prismatic SF [$SF3$; Figs. 8(e)–8(h)]. Two different $SF3$ are observed in Ti: the relatively shorter SF, connecting two basal SFs [Fig. 8(e)] in the region of variant α', and the longer SF, nucleating and growing within the region of parent α [Fig. 8(f)]. The former results from lattice reorientation, while the latter does not. Both prismatic SFs are the results of atomic slips along the $[1\bar{2}10]$ directions, leading to the change of stacking sequence from $\cdots$ABCDABCD$\cdots$ [Fig. 8(g)] to $\cdots$ABCDCDAB$\cdots$ [Fig. 8(h)] in view of the (0001) plane. The Burgers vector of prismatic SF is $1/3[1\bar{2}10]$, equal to that for the basal SF ($SF2$). However, different from $SF2$, the dissociation reaction of prismatic SF [51] can be expressed as

$$1/3[1\bar{2}10]_{SF3} \rightarrow 1/9[1\bar{2}10] + 2/9[1\bar{2}10]. \quad (12)$$

4. The α → ω phase transformation

Prompted by dislocation slips (basal and prismatic SFs), the phase transformation ($\alpha \rightarrow \omega$), induced by shock, then arises from GBs/GB junctions and grows towards the interior at the lower-impact velocities ($u_p \leqslant 1.0$ km s^{-1}), as shown in Fig. 9. What is the mechanism for such transformation? For nc-Ti in our simulations, both TAO-1 [Fig. 9(a)] and Silcock [Fig. 9(b)] mechanisms are observed to govern the shock-induced transformation, even within the grains with the same crystallographic orientation, i.e., B-type grains. However, the phase transformations are mostly observed to obey TAO-1 pathways, following the 90° lattice reorientation [$t = 10$ ps; Fig. 9(a)]. For TAO-1 transformation, it results from the emission and propagation of the basal (green) and prismatic (dark blue) SFs within the α' regions, during such lattice reorientation. Actually, such a transformation includes three steps: (i) shock impact boosts a local disordering within the region of α' [12 ps; Fig. 9(a)]; (ii) such disordering then triggers the basal and prismatic SFs; and (iii) the transformation nucleates and spreads outwards gradually, dragged by both groups of SFs [$t = 16$ ps; Fig. 9(a)]. The Silcock-governing transformation is a minority in shock-loaded nc-Ti, and no lattice reorientation arises for such transformation [$t = 21$ ps; Fig. 9(b)]. The transformation (Silcock) is also observed to

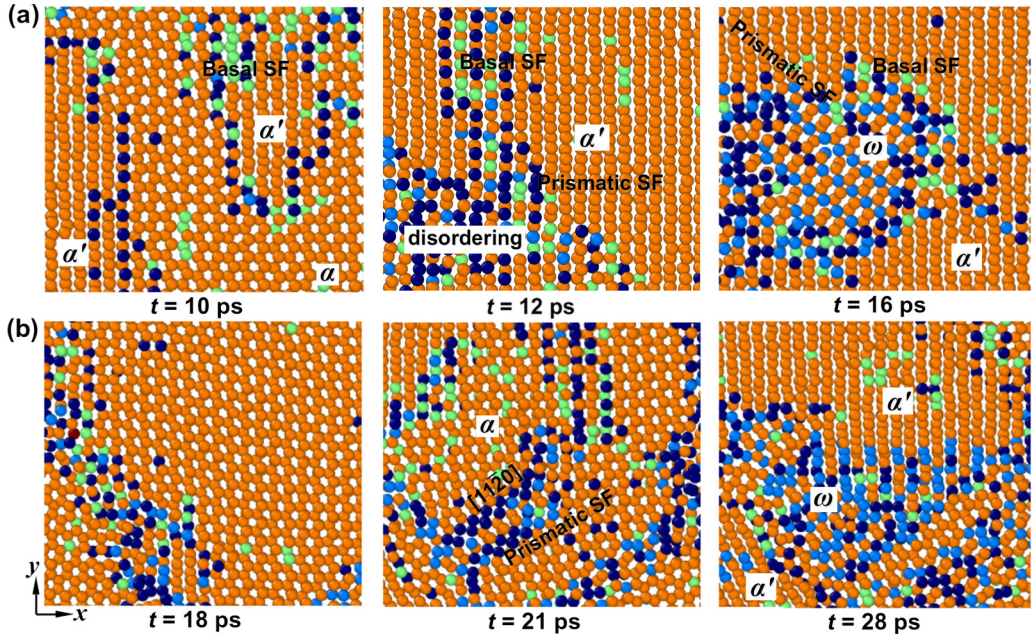

FIG. 9. Evolution of $\alpha \rightarrow \omega$ transformation, obeying the pathways of (a) $[1\bar{2}10]_\alpha//[10\bar{1}\bar{1}]_\omega$ and $(0001)_\alpha//(10\bar{1}1)_\omega$ (TAO-1) and (b) $(0001)_\alpha//(11\bar{2}0)_\omega$ and $[11\bar{2}0]_\alpha//[0001]_\omega$ (Silcock), within B-type grains, induced by shock compression. The cross sections are viewed along the z axis, and 6 × 6 nm on the xy plane.

stem from the $\{10\bar{1}0\}$ prismatic SFs [t = 28 ps; Fig. 9(b)] via the emission of slips in sequence along the $\langle 1\bar{2}10\rangle$ direction.

To describe the characteristics of both transformation mechanisms above, the simulated diffraction patterns, viewed along the z axis, are also applied. The transformation, obeying the TAO-1 pathway [Fig. 10(a)], triggers the coincidences for a few diffraction spots (e.g., α-0002 in pink and ω-10$\bar{1}$2 in green), but the appearance of many new diffraction spots (e.g., ω-0004 in green) is seen in the patterns. From the rotation angle between two spots (α-0002 and ω-0002), at about 30°, it is deduced that it satisfies an orientation relation of $(0001)_\alpha//(10\bar{1}1)_\omega$ between the α and ω phase [23]. Thus it is confirmed that such transformation (TAO-1) obeys the orientation relationships $[1\bar{2}10]_\alpha//[10\bar{1}\bar{1}]_\omega$ and $(0001)_\alpha//(10\bar{1}1)_\omega$. For the transformation governed by the Silcock mechanism [Fig. 10(b)], the diffraction pattern presents an apparent coincidence for a series of spots (e.g., α-$\bar{1}$100 and ω-10$\bar{1}$2), viewed in the xy plane, i.e., (0001) plane for α and $(1\bar{2}10)$ plane for ω. The same directions are observed for the spots of α-1$\bar{2}$10 and ω-0001, and it thus means a relation of

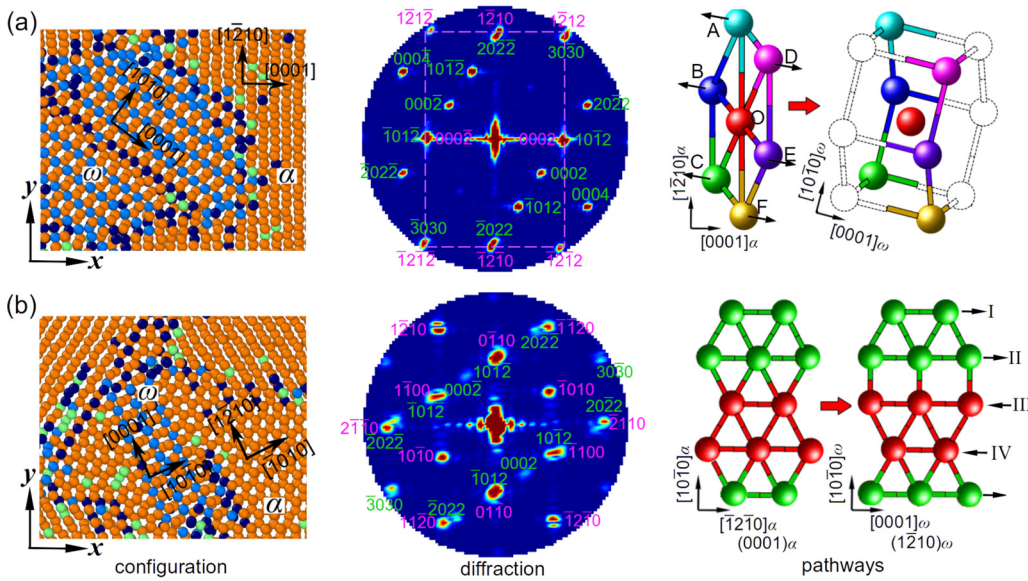

FIG. 10. Two mechanisms of $\alpha \rightarrow \omega$ phase transformation obeying the (a) TAO-1 and (b) Silcock pathways, respectively, in nc-Ti during shock compression. Their atomic configurations, the corresponding diffraction patterns (the indexes in pink and green represent α and ω phases, respectively), and the schematic diagrams of two transformation pathways are presented.

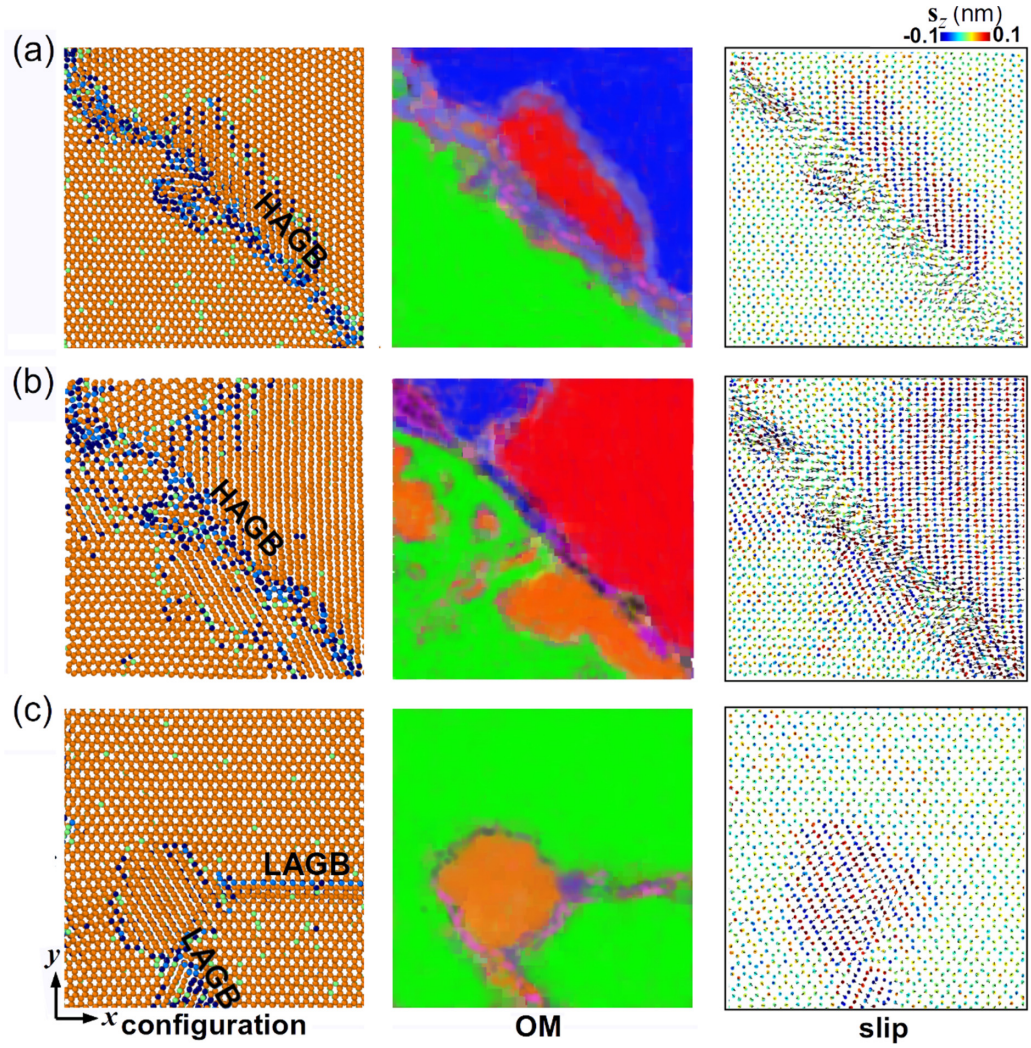

FIG. 11. Microstructural configurations showing plasticity (reorientation) in nc-Ti during shock compression, mediated by (a),(b) high-angle grain boundaries (HAGBs) and (c) low-angle grain boundaries (LAGBs).

$(0001)_\alpha//(1\bar{2}10)_\omega$ and $[1\bar{2}10]_\alpha//[0001]_\omega$, consistent with the previous MD [14] and experiment [11] results.

The pathways of both mechanisms (TAO-1 and Silcock) are also illustrated via the schematic diagrams shown in Fig. 10. For TAO-1, atomic shuffles are predominant [Fig. 10(a)]. During transformation, the basal plane, i.e., the (0001) plane of α, consisting of a series of hexagons surrounding individual atom (atom O), tends to break into two three-atom pieces (A–C and D–F atoms) [52]. Each three-atom piece swings in opposite directions out of the basal plane, which connects with the mated three-atom piece above or below. Then the honeycomb sublattice of ω is formed; simultaneously, another sublattice of ω is also formed by the remaining "unmoved" atoms. Such transformation induces the (0001) plane of α to transform into the $(01\bar{1}1)$ plane of ω. For the Silcock mechanism [Fig. 10(b)], the atomic shuffles are also involved in the transformation. In each basal plane, the atoms at I and II layers shuffle along the $[\bar{1}2\bar{1}0]$ direction, while other atoms at the two neighboring layers (III and IV) tend to shuffle in the opposite direction $[1\bar{2}10]$. Such repetitive processes facilitate the growth of the ω phase along this plane. In successive planes, the shuffles are presented to be opposite, and then create the $(1\bar{2}10)_\omega$ from $(0001)_\alpha$ [23]. Compared to the TAO-1 mechanism induced by atoms swinging, the transformation obeying the Silcock mechanism can be considered as the result of the relative slip of atoms.

5. Effects of GB and crystallographic orientation

The microstructural characteristics, i.e., the GBs and crystallographic orientation, play the key role in the deformation and transformation during impact. For the lattice reorientation, it almost originates from the GBs or GB junctions, and grows towards the interior (Fig. 11). In our simulations, two types of GBs, i.e., high-angle grain boundaries (HAGBs) and low-angle grain boundaries (LAGBs), are included in the nc-Ti. For HAGBs, the shock first facilitates GB gliding and then mediates apparent lattice rotations within B-type grains [Fig. 11(a)], along with the release of stresses [Figs. 4(c) and 4(d)]. Then another reorientation within A- or C-type grain is followed, due to GB sliding [Fig. 11(b)]. For LAGBs (GBs between A- and C-type grains), no GB sliding arises

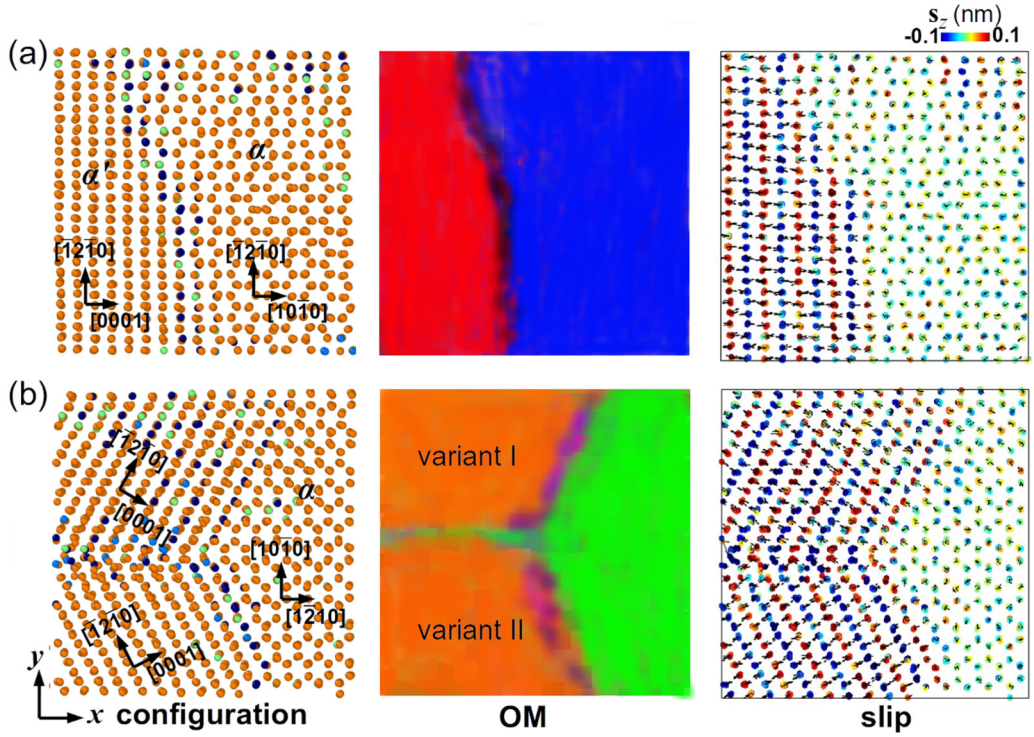

FIG. 12. Microstructural configurations showing the reorientation within grains in nanocrystalline Ti during shock compression. The cross sections for shock-induced reorientation lead to (a) one variant of α')-HCP within B-type grains and (b) two variants (I and II) within A- or C-type grains. The microstructural deformation is also characterized with OM and slip vectors ($\mathbf{s}_z$). The cross section is viewed along the z axis, and 4 × 4 nm on the xy plane. The arrows show the slip directions.

owing to the stability of such GBs, but plasticity, i.e., lattice reorientation, originates from the GB junctions and grows along the GB planes within A- or C-type grains, under shock loading [Fig. 11(c)]. The lattice reorientation also presents an apparent crystallographic dependence. For example, shock-induced lattice reorientation prompts one type of rotated [0001] α' variant within shocked B-type grains [Fig. 12(a)], but two different types of rotated [0001] α' variants within A- or C-type grains [Fig. 12(b)]. The difference can be illustrated that the [$1\bar{2}10$] shock direction forces the parent α hcp rotating to α' hcp in two ways: [$1\bar{1}00$] $\alpha \rightarrow$ [0001] α' and [$0\bar{1}10$] $\alpha \rightarrow$ [0001] α', respectively. Between two variants, i.e., I and II [Fig. 12(b)], the misorientation angle is rounded to 60°. The boundaries between two rotated variants is CTB, different from the ones between rotated α' and parent α regions, i.e., IPBs.

Such orientation effects on plasticity can be explained with resolved shear stress (RSS, in Table I), which is a key quantity for dislocation or twinning nucleation. During shock compression, lattice reorientation results from one of three slip systems: ($1\bar{1}02$)[$1\bar{1}01$], ($01\bar{1}2$)[$01\bar{1}1$], and ($10\bar{1}2$)[$10\bar{1}1$] (Fig. 13). Their RSS is different in the grains with different crystallographic orientation. Within A- or C-type grains (shock along the $\langle 1\bar{2}10\rangle$ directions), the RSS of the slip system ($10\bar{1}2$)[$10\bar{1}1$] is smaller than the other two slip systems (0.68 ≪ 7.26 or 7.55 GPa), i.e., the ($10\bar{1}2$)[$10\bar{1}1$] slip system is more difficult to activate in A- or C-type grains [Fig. 12(b)], while the RSS of slip system ($10\bar{1}2$)[$10\bar{1}1$] is much larger (∼11.43 GPa) than that for other slip systems within B-type grains, so only one variant α', via prompting the activation of the ($10\bar{1}2$)[$10\bar{1}1$] slip system, is observed [Fig. 12(a)].

The phase transformation, induced by shock compression, is also strongly dependent on the characteristics of GBs and crystallographic orientations. In nanocrystalline Ti, the $\alpha \rightarrow \omega$ phase transformation governed by the TAO-1 mechanism [Figs. 9(a) and 10(a)] arises preferentially within B-type grains [Figs. 3(a) and 3(b)]. Such transformation is observed to originate from HAGBs, where stresses tend to congregate and GB sliding boosts the plasticity and phase transformation. GB sliding tends to arise heterogeneously and spread within B-type grains [Fig. 11(a)], which facilitate plasticity and the release of stress [Figs. 4(c) and 4(d)]. Then the swinging rather than relative slips of atoms can be activated easily, i.e., within B-type grains, and thus the TAO-1 mechanism governs

TABLE I. Resolved shear stresses (RSS) in shocked nc-Ti, for selected slip systems and grains with different crystallographic orientation.

Grain type	Shock plane	Slip system	RSS (GPa)	Emission
A/C	($1\bar{2}10$)	($1\bar{1}02$)[$1\bar{1}01$]	7.55	Y
		($01\bar{1}2$)[$01\bar{1}1$]	7.26	Y
		($10\bar{1}2$)[$10\bar{1}1$]	0.68	N
B	($10\bar{1}0$)	($1\bar{1}02$)[$1\bar{1}01$]	4.52	N
		($01\bar{1}2$)[$01\bar{1}1$]	4.63	N
		($10\bar{1}2$)[$10\bar{1}1$]	11.43	Y

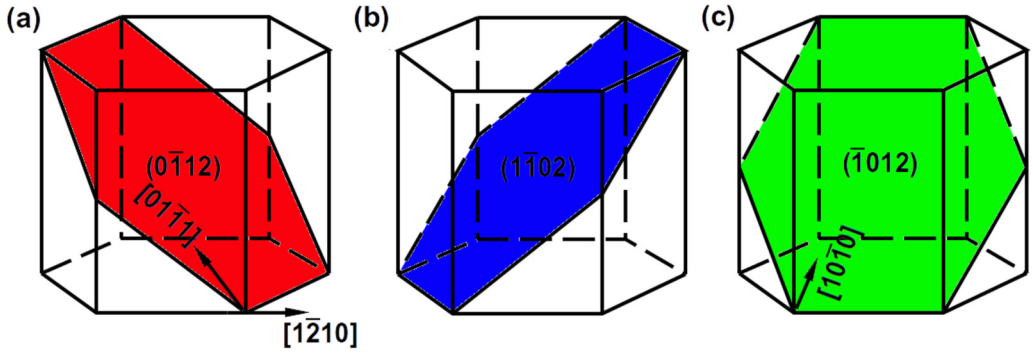

FIG. 13. Schematic illustrations for three slip systems for deformation twins in hcp-Ti: (a) (0$\bar{1}$12)[0$\bar{1}$11], (b) (1$\bar{1}$02)[1$\bar{1}$01], and (c) ($\bar{1}$012)[$\bar{1}$011].

the phase transformation, although minor Silcock-governing transformation also arises [Fig. 9(b)]. However, in A- or C-type grains, the transformation governed by the Silcock mechanism [Fig. 10(b)] tends to be delayed and nucleates within the grain interior. Within the grain interior, the higher stresses remain after plasticity and prompt the emergence of atomic slips, i.e., prismatic SFs, which facilitate the emission and evolution of the $\alpha \rightarrow \omega$ phase transformation obeying the Silcock mechanism [Fig. 9(b)].

In nanocrystalline Ti, shock-induced disordering is another important deformation mode. When $u_p \geqslant 1.5$ km s^{-1}, the "solid-state" disordering is dominated during shock compression. Surprisingly, this solid-state disordering also shows an orientation dependence at $u_p = 1.5$ km s^{-1} [Fig. 3(c)]. Following the plasticity, i.e., lattice reorientation within grain interior [Fig. 14(a)], disordering is observed to preferentially occur at GBs and within the interiors of A- and C-type grains [Fig. 14(b)]. The disordering tends to spread along GBs and within A- or C-type grains, and then invade B-type grains [Figs. 14(c) and 14(d)], although they present some resistances to amorphization. Such anisotropy in the disordering is due to the different stresses within A-/C- and B-type grains (Fig. 4). After plastic deformation, i.e., lattice reorientation, the stresses that remain in A- or C-type grains are higher than that in B-type grains, and thus the catastrophic, homogeneous activation of slip systems and their interactions prefers to arise within the interior of A- or C-type grains, which accelerates solid-state disordering [44].

B. Release and tension stage

1. The $\omega \rightarrow \alpha$ reversed transformation

The reversed transformation of $\omega \rightarrow \alpha$, commonly seen in Zr experimentally [53], is observed as the release wave passes (Fig. 15). What are the mechanisms for such reversed transformation, and do the forward and reverse transformations share

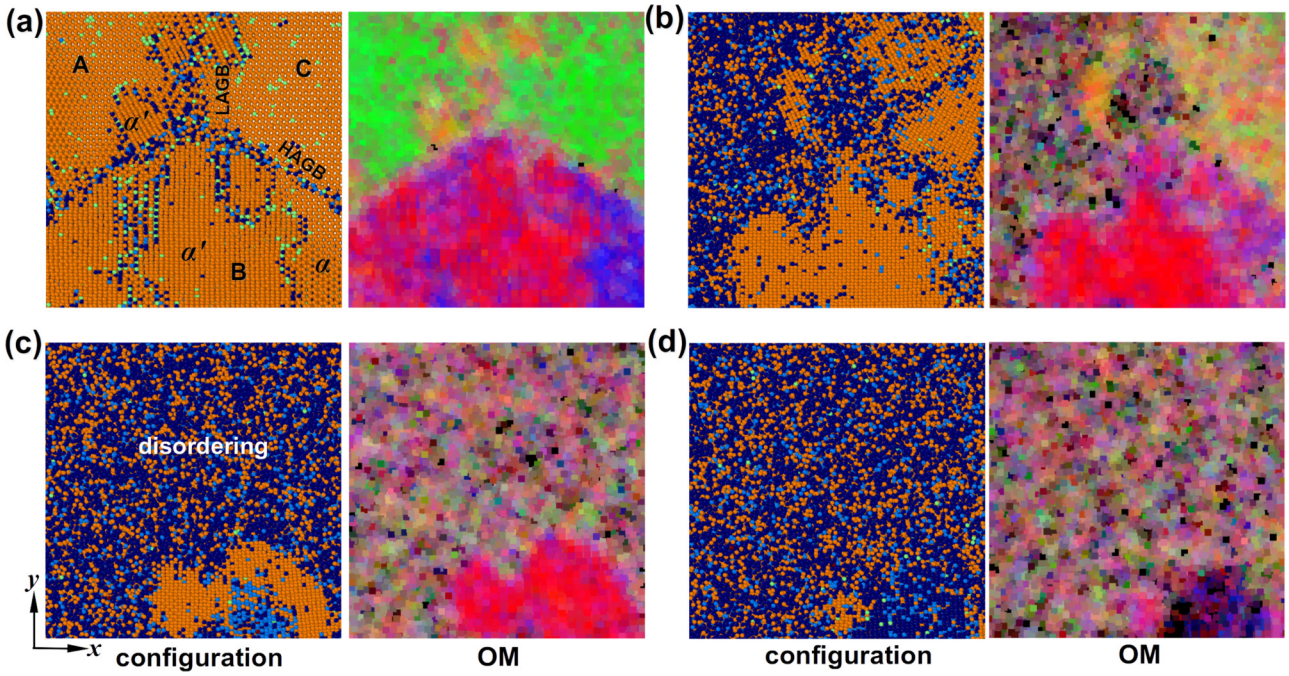

FIG. 14. Shock-induced disordering for columnar nanocrystalline Ti: Deformation evolution at $t =$ (a) 8 ps, (b) 12 ps, (c) 15 ps, and (d) 25 ps. The impact velocity u_p is 1.5 km s^{-1}.

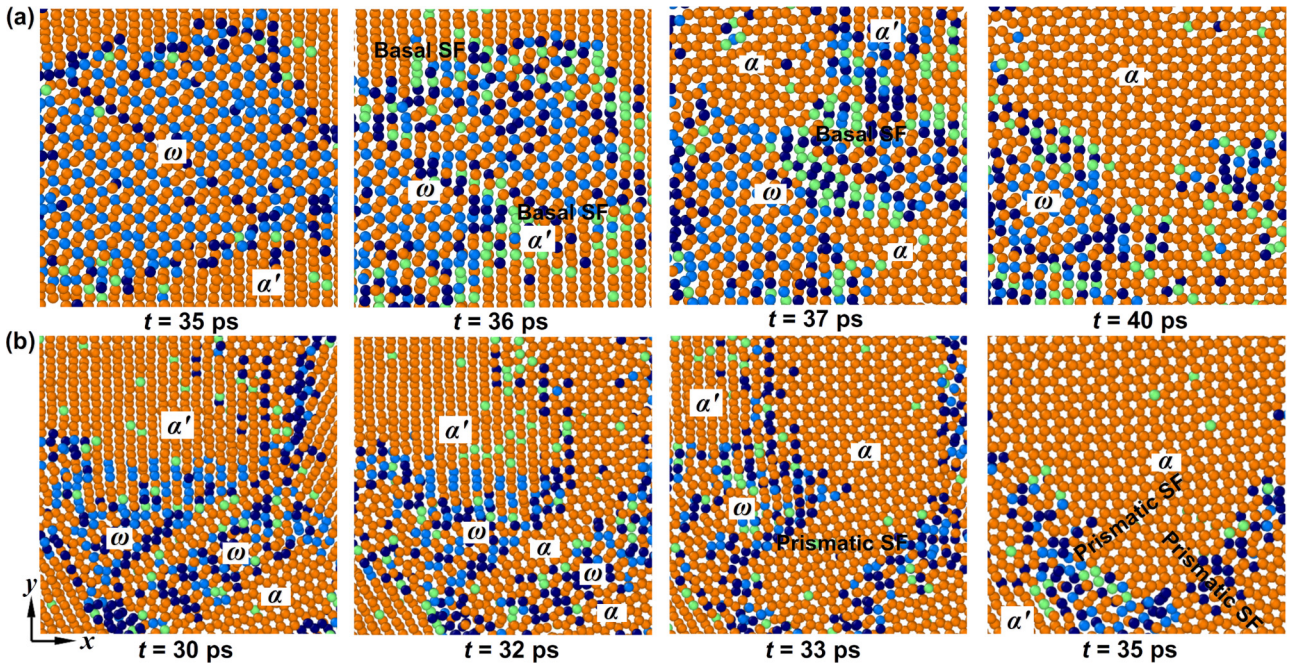

FIG. 15. Sequence showing the reversed $\omega \rightarrow \alpha$ transformation during the release stage, obeying the pathways of (a) TAO-1 and (b) Silcock, respectively. The cross sections are viewed along the y axis, and 10×10 nm on the xz planes.

a similar mechanism? The previous experiments for Ti under shock [8] or split Hopkinson bar loading [9] by analyzing the postmortem microstructures cannot acquire such reversed $\omega \rightarrow \alpha$ transformation induced by release because shocks are rapid and adiabatic [22]. Our simulation results present a similar mechanism for $\alpha \rightarrow \omega$ and $\omega \rightarrow \alpha$ transformation, i.e., the same orientation relations are observed to obey for both TAO-1 [Fig. 15(a)] and Silcock [Fig. 15(b)] transformation as well as the reversed processes. For instance, when the release wave passes, it presents an apparent shrinking of the ω-structured Ti, corresponding to a recovery of α' prompted by the propagation of basal and prismatic SFs [$t = 36$ ps; Fig. 15(a)], after a TAO-1 transformation within B-type grains [$t = 35$ ps; Fig. 15(a)]. Following the $\omega \rightarrow \alpha$ transformation, a reversed 90° lattice reorientation, which cannot be observed for the reversed Silcock-governing transformation [Fig. 15(b)], is followed and forces a rotation from [0001] α' to $[10\bar{1}0]$ α hcp [$t = 37$ ps; Fig. 15(a)]. Interestingly, there still exists some ω-structured Ti remaining in the grains ($\sim$4.8% $\ll$ 16.0% for the maximum value of ω Ti) even at the completed release stage [40 ps; Fig. 15(a)], and the orientation relations between the α and ω phases are $(0001)_\alpha//(11\bar{2}0)_\omega$ and $[11\bar{2}0]_\alpha//[0001]_\omega$, which is in accordance with the postmortem experiments of Ti under shock loading [11]. Such results for the reversed transformation demonstrate that it is insufficient to determine the mechanisms or pathways for the transformation via simply contrasting the postmortem microstructures with untested ones in experiments, and thus an ultrafast and time-resolved determination is necessary.

2. The spallation

When two release fans interact with each other, it triggers a tension and the subsequent spallation in the nanocrystalline Ti. Figure 16 exhibits the evolution of spallation for nc-Ti at the released state [Fig. 16(a)] and increasing tension states [Figs. 16(b)–16(d)] in terms of orientation maps. During release and, subsequently, tension, the reversed plasticity, e.g., lattice reorientations ($\alpha' \rightarrow \alpha$), are partially [Fig. 16(a)] and completely [Fig. 16(b)] involved. The variant α', due to the lattice rotation at the compression stage, almost disappears, which implies a structural recovery. Such recovery leads to an apparent orientation change at fine scales, as characterized via orientation maps. Simultaneously, more stacking faults, i.e., $1/3[1\bar{2}10]$ basal and prismatic SFs, are observed within B-type grains [Fig. 16(b)] due to a local stress concentration, during the tension. As tensile loading progresses, the pronounced GB deformation, i.e., GB sliding and GB-mediated basal/prismatic SFs, takes place and spread towards A- or C-type grains. Then they would evolve into a series of deformation "bands" within the grains [Fig. 16(c)]. During tension, GBs/GB junctions, where local stress preferentially releases, are the source of plasticity [40]. Then it prompts disordering owing to the plasticity, GB deformation, and their interactions. Such disordering facilitates the void nucleation and growth [Fig. 16(d)], which is consistent with previous experimental and simulation results [54,55]. Meanwhile, the void nucleation and growth can reversely affect the plasticity in dynamics. The voids formed can accelerate the plasticity nucleation, but inhibit their propagations. Thus, around the voids, the locally crystallographic orientation is observed to be changed [Fig. 16(d)], owing to the change of local stress conditions, as the ensuing plasticity increasing.

C. Discussion

Our simulations on shock-loaded nc-Ti present apparently different mechanisms of $\alpha \rightarrow \omega$ transformation, i.e., TAO-1

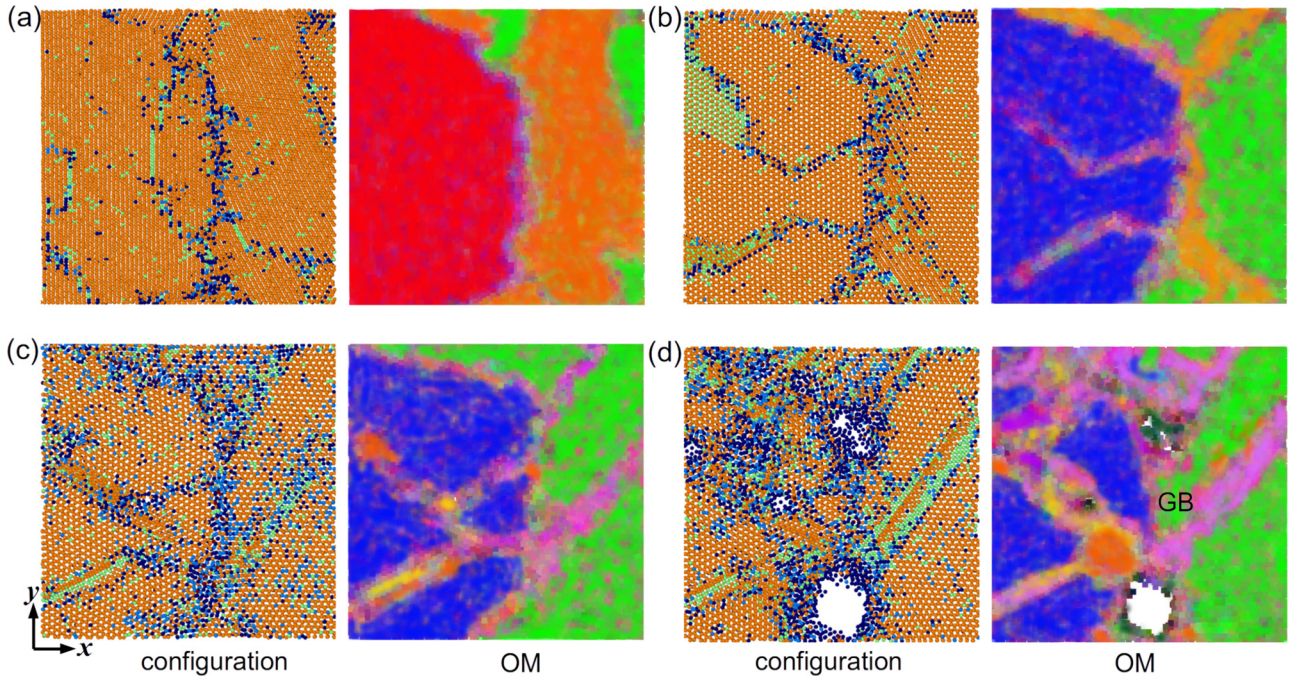

FIG. 16. Deformation and spallation of hexagonal nc-Ti around a GB triple junction during release and tension stages, and the corresponding orientation maps.

and Silcock, from that for Zong's MD simulations [14,24], i.e., Silcock. Such different mechanisms can be attributed to the effects of GBs and the dislocation slips mediated by GBs. For Silcock-governing transformation, the GB presents a strong inhibition: the Silcock-governing transformation tends to activate in single crystals (Fig. 1(d) [14]) or within the grain interiors because the remaining higher stresses prompt the $[1\bar{2}10](10\bar{1}0)$ prismatic SFs to facilitate the formation of ω-structured Ti via dragging the relative slip of atoms. In our simulations, GBs, especially HAGBs, contribute to the basal and prismatic SFs in shocked nc-Ti and accelerate the release of stress. Thus, TAO-1, driven by atom shuffles, is governing the transformation originated from the GBs.

Comparing our simulation results with the experimental analysis by TEM [11], it also presents the different transformation mechanisms, even for the shocked polycrystal (coarse-grained) Ti. The diffraction pattern, based on TEM analysis in experiment, shows an orientation relationship for the α and ω phases: $(0001)_\alpha//(\bar{1}2\bar{1}0)_\omega$ and $[\bar{1}\bar{1}20]_\alpha//[0001]_\omega$, obeying Silcock mechanisms. Such difference can result from the modes of experimental measurement. For Cerreta's experiment, the postmortem microstructural analysis was performed in Ti crystals and the dynamic process cannot be acquired. In fact, repeated processes of $\alpha \rightarrow \omega$ and reversed $\omega \rightarrow \alpha$ were involved in the samples of Ti before the TEM measurements, which hinders the awareness of transformation mechanisms. Along the reversed transformation of $\omega \rightarrow \alpha$, our MD simulation demonstrated that it undergoes a reversed lattice reorientation, i.e., $\alpha' \rightarrow \alpha$, prompting the coexistence of α and remaining ω phases in final, with the orientation relationship of $(0001)_\alpha//(1\bar{2}10)_\omega$ and $[1\bar{2}10]_\alpha//[0001]_\omega$ [$t =$ 40 ps; Fig. 15(a)], after the release stage. By analyzing the final shocked samples, the same orientation relationship of the α and ω phases is obtained in both the simulations and experiments.

The discussion above indicates that if the information/details of structural changes in dynamics are neglected for a shock-induced phase transformation, it will give rise to misleading conclusions. The recent development of *in situ* and high-resolution temporal and spatial probes, i.e., femtosecond x-ray diffraction (XRD) using a x-ray free-electron laser (XFEL), provides an excellent method or opportunity to determine the underlying mechanisms of $\alpha \rightarrow \omega$ transformation in experiments. Swinburne *et al.* [22] performed femtosecond XRD to study the shock response of polycrystalline Zr, and found a clear orientation relationship of $(10\bar{1}0)_\alpha//(10\bar{1}1)_\omega$ (TAO-1 transformation) during $\alpha \rightarrow \omega$ transformation. The experimental findings are in agreement with our simulations, although the shocked materials are different, i.e., Zr for the *in situ* XRD experiments and Ti for MD simulations, respectively. Fortunately, such differences would not interfere with the knowledge of the transformation in Ti because previous experiment studies, mainly the TEM analysis, indicate that the phase transformation behaviors are similar for Zr and Ti [7,11,56,57]. We expect future experimental studies, applying femtosecond XRD analysis, to confirm such similarities in Zr and Ti, and validate our predictions on the shock-induced transformation of Ti, i.e., the single and polycrystals.

IV. CONCLUSION

Using NEMD, we studied the deformation and spallation damage induced by shock compression and subsequent tension in hexagonal columnar nanocrystalline Ti. The main conclusions are listed below:

(a) Anisotropy in the propagation of a shock-induced plastic wave in nanocrystalline Ti is significant at lower impact strength. The anisotropy tends to be weakened, and even annihilated, with the increase of impact velocity ($u_p \geqslant 1.5$ km s^{-1}).

(b) Shock-induced deformation first undergoes a heterogeneous plasticity, including the 90° lattice reorientation and dislocation slips, within the grains; and then a heterogeneous $\alpha \rightarrow \omega$ phase transformation at lower impact velocities, or a homogeneous solid-state disordering at higher impact velocities. The plasticity or phase transformation prefers to nucleate at GBs/GB junctions, and exhibits a strong dependence on crystallographic orientation.

(c) The 90° lattice reorientation is the coupling effects of deformation twinning and slips, driven by atomic shuffles and atomic glides, respectively, under shock loading. Most of $\alpha \rightarrow \omega$ transformations originated from GBs are governed by the TAO-1 mechanism, while a few are driven by the Silcock mechanism within the grain interiors. The transformations governed by the TAO-1 and Silcock mechanisms stem from the emission and propagation of basal-prismatic and prismatic stacking faults, respectively.

(d) The release and tension of wave facilitates the reversed $\omega \rightarrow \alpha$ transformation, structural recovery, and subsequent spallation of nanocrystalline Ti. The reversed transformation of $\omega \rightarrow \alpha$ is driven by the similar mechanisms with transformation of $\alpha \rightarrow \omega$. The spallation preferentially occurs at GB or the intersection of plasticity, and also prompts the plasticity and orientation change.

ACKNOWLEDGMENTS

This work was partially supported by the NSFs of China (Grants No. 11672254 and No. 11802092), the Scientific Innovation Program of Hunan Agricultural University (Grant No. 2018ZK13), the Young Scholar of Hunan Agricultural University (Grant No. 17QN22), and the Science and Technology Foundation of State Key Laboratory of Shock Wave and Detonation Physics (Grant No. LSB-KB1804). We also acknowledge the support of the computation platform of the National Super Computer Center in Changsha (NSCC).

[1] A. S. Khan and H. W. Liu, Int. J. Plast. **37**, 1 (2012).
[2] Z. W. Wyatt, W. J. Joost, D. Zhu, and S. Ankem, Int. J. Plast. **39**, 119 (2012).
[3] T. Hama, A. Kobuki, and H. Takuda, Int. J. Plast. **91**, 77 (2017).
[4] B. Feng and V. I. Levitas, Int. J. Plast. **96**, 156 (2017).
[5] D. Fan, J. W. Huang, X. L. Zeng, Y. Li, J. C. E, J. Y. Huang, T. Sun, K. Fezzaa, Z. Wang, and S. N. Luo, Rev. Sci. Instrum. **87**, 053903 (2016).
[6] B. Feng, C. A. Bronkhorst, F. L. Addessio, B. M. Morrow, E. K. Cerreta, T. Lookman, R. A. Lebensohn, and T. Low, J. Mech. Phys. Solids **119**, 274 (2018).
[7] E. Cerreta, G. T. Gray III, R. S. Hixson, P. A. Rigg, and D. W. Brown, Acta Mater. **53**, 1751 (2005).
[8] D. R. Jones, B. M. Morrow, C. P. Trujillo, G. T. Gray III, and E. K. Cerreta, J. Appl. Phys. **122**, 045902 (2017).
[9] B. M. Morrow, R. A. Lebensohn, C. P. Trujillo, D. T. Martinez, F. L. Addessio, C. A. Bronkhorst, T. Lookman, and E. K. Cerreta, Int. J. Plast. **82**, 225 (2016).
[10] P. Zhou, S. Xu, D. W. Xiao, C. L. Jiang, and J. Wang, Int. J. Plast. **112**, 194 (2019).
[11] E. Cerreta, G. T. Gray III, A. C. Lawson, T. A. Mason, and C. E. Morris, J. Appl. Phys. **100**, 013530 (2006).
[12] H. Wang, P. D. Wu, J. Wang, and C. N. Tome, Int. J. Plast. **49**, 36 (2013).
[13] S. R. Niezgoda, A. K. Kanjarla, I. J. Beyerlein, and C. N. Tomé, Int. J. Plast. **56**, 119 (2014).
[14] H. X. Zong, T. Lookman, X. D. Ding, S. N. Luo, and J. Sun, Acta Mater. **65**, 10 (2014).
[15] D. H. Kalantar, J. F. Belak, G. W. Collins, J. D. Colvin, H. M. Davies, J. H. Eggert, T. C. Germann, J. Hawreliak, B. L. Holian, K. Kadau, P. S. Lomdahl, H. E. Lorenzana *et al.*, Phys. Rev. Lett. **95**, 075502 (2005).
[16] K. Wang, S. F. Xiao, H. Q. Deng, W. J. Zhu, and W. Y. Hu, Int. J. Plast. **59**, 180 (2014).
[17] K. Wang, W. J. Zhu, S. F. Xiao, K. G. Chen, H. Q. Deng, and W. Y. Hu, Int. J. Plast. **71**, 218 (2015).
[18] K. Wang, J. Chen, W. J. Zhu, W. Y. Hu, and M. Z. Xiang, Int. J. Plast. **96**, 56 (2017).
[19] P. A. Rigg, C. W. Greff, M. D. Knudson, G. T. Gray, and R. S. Hixson, J. Appl. Phys. **106**, 123532 (2009).
[20] E. K. Cerreta, J. P. Escobedo, P. A. Rigg, C. P. Trujillo, D. W. Brown, T. A. Sisneros, B. Clausen, M. F. Lopez, T. Lookman, C. A. Bronkhorst, and F. L. Addessio, Acta Mater. **61**, 7712 (2013).
[21] D. W. Brown, J. D. Almer, L. Balogh, E. K. Cerreta, B. Clausen, J. P. Escobedo-Diaz, T. A. Sisneros, P. L. Mosbrucker, E. F. Tulk, and S. C. Vogel, Acta Mater. **67**, 383 (2014).
[22] T. D. Swinburne, M. G. Glavicic, K. M. Rahman, N. G. Jones, J. Coakley, D. E. Eakins, T. G. White, V. Tong, D. Milathianaki, G. J. Williams, D. Rugg, A. P. Sutton *et al.*, Phys. Rev. B **93**, 144119 (2016).
[23] D. R. Trinkle, R. G. Hennig, S. G. Srinivasan, D. M. Hatch, M. D. Jones, H. T. Stokes, R. C. Albers, and J. W. Wilkins, Phys. Rev. Lett. **91**, 025701 (2003).
[24] H. Zong, X. Ding, T. Lookman, J. Li, J. Sun, E. K Cerreta, J. P. Escobedo, F. L. Addessio, and C. A. Bronkhorst, Phys. Rev. B **89**, 220101(R) (2014).
[25] R. J. McCabe, G. Proust, E. K. Cerreta, and A. Misra, Int. J. Plast. **25**, 454 (2009).
[26] F. Zhao, L. Wang, D. Fan, B. X. Bie, X. M. Zhou, T. Suo, Y. L. Li, M. W. Chen, C. L. Liu, M. L. Qi, M. H. Zhu, and S. N. Luo, Phys. Rev. Lett. **116**, 075501 (2016).
[27] M. Battaini, E. V. Pereloma, and C. Davies, Metallurg. Mater. Trans. A **38**, 276 (2007).
[28] L. Wang, F. Zhao, F. P. Zhao, Y. Cai, Q. An, and S. N. Luo, J. Appl. Phys. **115**, 053528 (2014).
[29] L. Wang, J. C. E, Y. Cai, F. Zhao, D. Fan, and S. N. Luo, J. Appl. Phys. **117**, 084301 (2015).
[30] J. A. Hawreliak, B. EI-Dasher, H. Lorenzana, G. Kimminau, A. Higginbotham, B. Nagler, S. M. Vinko, W. J. Murphy, T. Whitcher, J. S. Wark, S. Rothman, and N. Park, Phys. Rev. B **83**, 144114 (2011).

[31] S. Plimpton, J. Comput. Phys. **117**, 1 (1995); also see http://lammps.sandia.gov (unpublished).
[32] R. G. Hennig, T. J. Lenosky, D. R. Trinkle, S. P. Rudin, and J. W. Wilkins, Phys. Rev. B **78**, 054121 (2008).
[33] M. Ghazisaeidi and D. R. Trinkle, Acta Mater. **60**, 1287 (2012).
[34] C. Woodward, D. R. Trinkle, L. G. Hector, Jr., and D. L. Olmsted, Phys. Rev. Lett. **100**, 045507 (2008).
[35] S. P. Marsh, *LASL Shock Hugoniot Data* (University of California Press, Berkeley, 1980).
[36] S. Eliezer, I. Cilath, and T. Bar-Noy, J. Appl. Phys. **67**, 715 (1990).
[37] J. M. Silcock, Acta Metall. **6**, 481 (1958).
[38] T. G. Desai, P. C. Millett, and D. Wolf, Acta Mater. **56**, 4489 (2008).
[39] B. L. Holian and P. S. Lomdahl, Science **80**, 2085 (1998).
[40] S. N. Luo, Q. An, T. C. Germann, and L. B. Han, J. Appl. Phys. **106**, 013502 (2009).
[41] G. J. Ackland and A. P. Jones, Phys. Rev. B **73**, 054104 (2006).
[42] J. F. Tang, J. C. Xiao, L. Deng, W. Li, X. M. Zhang, L. Wang, S. F. Xiao, H. Q. Deng, and W. Y. Hu, Phys. Chem. Chem. Phys. **20**, 28039 (2018).
[43] V. Randle and O. Engler, *Introduction of Texture Analysis Macrotexture, Microtexture and Orientation Mapping* (CRC Press, Boca Raton, FL, 2000).
[44] L. Wang, Y. Cai, A. M. He, and S. N. Luo, Phys. Rev. B **93**, 174106 (2016).
[45] D. R. Chichili, K. T. Ramesh, and K. J. Hemker, Acta Mater. **46**, 1025 (1998).
[46] C. D. Barrett, H. EI Kadiri, and M. A. Tschopp, J. Mech. Phys. Solids **60**, 2084 (2012).
[47] L. Lu, B. X. Bie, Q. H. Li, T. Sun, K. Fezzaa, X. L. Gong, and S. N. Luo, Acta Mater. **132**, 389 (2017).
[48] A. Ishii, J. Li, and S. Ogata, Int. J. Plast. **82**, 32 (2016).
[49] X. Y. Zhang, B. Li, and Q. Liu, Acta Mater. **90**, 140 (2015).
[50] P. Chen, F. X. Wang, and B. Li, Acta Mater. **164**, 440 (2019).
[51] A. Akhtar and E. Teghtsoonian, Metal. Trans. A **6**, 2201 (1975).
[52] D. R. Trinkle, D. M. Hatch, H. T. Stokes, R. G. Hennig, and R. C. Albers, Phys. Rev. B **72**, 014105 (2005).
[53] B. M. Morrow, J. P. Escobedo, R. D. Field, R. M. Dickerson, P. O. Dickerson, C. P. Trujillo, and E. K. Cerreta, AIP Conf. Proc. **1793**, 100033 (2017).
[54] Y. Ashkenazy and R. S. Averback, Appl. Phys. Lett. **86**, 051907 (2005).
[55] S. G. Srinivasan, M. I. Baskes, and G. J. Wagner, J. Appl. Phys. **101**, 043504 (2007).
[56] S. K. Sikka, Y. K. Voar, and R. Chidambaram, Prog. Mater. Sci. **27**, 245 (1982).
[57] H. R. Wenk, P. Kaercher, W. Kanitpanyacharoen, E. Zepeda-Alarcon, and Y. Wang, Phys. Rev. Lett. **111**, 195701 (2013).